**LETTER**

# Inkjet printable-photoactive all inorganic perovskite films with long effective photocarrier lifetimes

# Letter

# Inkjet printable-photoactive all inorganic perovskite films with long effective photocarrier lifetimes

C C Ilie[1], F Guzman[2], B L Swanson[1], I R Evans[1], P S Costa[3], J D Teeter[4], M Shekhirev[4], N Benker[3], S Sikich[5], A Enders[6], P A Dowben[3], A Sinitskii[4] and A J Yost[3]

[1] Department of Physics, State University of New York-Oswego, Oswego, NY 13126-3599, United States of America
[2] Department of Physics, California State University-San Bernardino, San Bernardino, CA 92407-2318, United States of America
[3] Department Physics and Astronomy, University of Nebraska-Lincoln, Lincoln, NE 68588-0299, United States of America
[4] Department of Chemistry, University of Nebraska-Lincoln, Lincoln, NE 68588-0304, United States of America
[5] Department of Chemistry, Doane University, Crete, NE 68333, United States of America
[6] Physikalisches Institut, Universität Bayreuth, Bayreuth, Germany

E-mail: ayost3@unl.edu

## Abstract

Photoactive perovskite quantum dot films, deposited via an inkjet printer, have been characterized by x-ray diffraction and x-ray photoelectron spectroscopy. The crystal structure and bonding environment are consistent with $CsPbBr_3$ perovskite quantum dots. The current–voltage ($I$–$V$) and capacitance–voltage ($C$–$V$) transport measurements indicate that the photo-carrier drift lifetime can exceed 1 ms for some printed perovskite films. This far exceeds the dark drift carrier lifetime, which is below 50 ns. The printed films show a photocarrier density $10^9$ greater than the dark carrier density, making these printed films ideal candidates for application in photodetectors. The successful printing of photoactive-perovskite quantum dot films of $CsPbBr_3$, indicates that the rapid prototyping of various perovskite inks and multilayers is realizable.

Keywords: inkjet printing, inorganic perovskite, nanoparticle inks, nanoparticles, photovoltaics, carrier lifetime

(Some figures may appear in colour only in the online journal)

## Introduction

Halide-based perovskite solar cells (HPSCs) have recently drawn considerable attention due to their low cost, extraordinary power conversion efficiency, and long carrier lifetimes and diffusion lengths. The efficiency of the solar cells using organic–inorganic-based perovskites increased from 3.8% in 2009 to over 22% in 2016 [1, 2]. In spite of the impressive performance of the hybrid organic based HPSCs, these organic halide perovskites have a number of drawbacks including sensitivity to heat, moisture, and radiation induced degradation [3]. An alternative approach is the use of wholly inorganic based HPSC materials, as a way of circumventing some of the drawbacks of the organic based HPSCs.

Device performance of the inorganic HPSCs has also seen dramatic improvements from a device efficiency of 0.9% for a layered solar cell structure of $CsSnI_3$ deposited by a solution based method, as reported in a 2012 study [4]. By 2014, Kumar *et al* [5] adopted the use of a mesoporous $TiO_2$ scaffold and doped $CsSnI_3$ with $SnF_2$ in order to increase the device efficiency to 2%. Then in 2016, Swarnkar *et al* [6] employed $CsPbI_3$ quantum dots, utilizing the concept of surface passivation through a dip-coating methodology, to drastically improve device efficiency to 10.77%. More recently, in early 2017, it was shown that using a mixed halide perovskite, namely $CsPbI_2Br$, and a vapor deposition method can boost device performance to 11.8% [7]. Finally, in late 2017, Sanehira *et al* used a post-treatment of formamidinium iodide salt solution to coat $CsPbI_3$ quantum dot films, which resulted in a stabilized device efficiency of 13.43% [8].

In addition to device efficiency, the effective carrier lifetimes have also steadily increased for the inorganic halide-based perovskite materials. In 2015, Yantara *et al* [9] reported lifetimes on the order of 4.0 ns for a solution processed $CsPbBr_3$ light emitting diode device structure. The lifetime then increased by more than seven times to 30 ns when Rakita *et al* [10] grew millimeter sized single crystal $CsPbBr_3$ in 2016. Then in 2017, Hutter *et al* [11] used vapor deposited $CsPbI_3$ to achieve effective charge carrier lifetimes on the order of 50 $\mu$s.

Although the performance has not increased as significantly as the organic–inorganic halide perovskites, quantum dots of the inorganic halide-based perovskites are highly desirable candidates as solar cell materials as they have high optical absorption coefficients and they possess direct bandgaps which can be tuned through quantum dot (QD) particle size and stoichiometric manipulation of the halides [12, 13]. The inorganic HPSCs, specifically $CsPbX_3$ (X = Br, Cl, I), can also be synthesized to have a uniform size and stable emission which is favorable for quantum dot displays [12–15]. Furthermore, the inorganic HPSCs are more robust compared to the organic HPSCs, with regard to environmental sensitivity [16]. Interestingly, the inorganic HPSCs have found many uses related to light emitting diodes [17–21], lasers [22–29], photo detection [30–33], high energy radiation detection [34], and of course photovoltaic applications [4–7, 11, 35–38].

Since the first reported use of inkjet printing in solar cells in 1987, scientists have sought ways to successfully print an all inorganic solar cell with attractive performance properties [39]. The inkjet printing method uses solution based materials as inks and has many advantages compared to vacuum based deposition methods. Inkjet printing allows for printing in atmospheric conditions, printing large areas on flexible substrates, low temperature processing, higher efficiency of material usage, print by design i.e. tailored patterning, mass production, and non-contact deposition [40, 41].

Although inorganic perovskites are more suitable for use, overcoming many of the deficiencies of the organic HPSCs, polycrystalline Si (poly-Si) remains the most competitive and commercially viable solar cell material [40, 42]. Currently the best performing commercially available photovoltaics are based on poly-Si [40, 42]. Poly-Si and other leading photovoltaic materials require vacuum-based fabrication methods, suffer from poor scalability [40, 41], and are not 'printable' materials. The printed poly-Si results in numerous grain boundaries which result in trap sites for carriers and thus lead to poor device performance [40–42]. Furthermore, the printed poly-Si film will require high temperature post treatment which prohibits the use of cheap flexible substrates and generally is not cost effective [40–42] as there are huge hazards associated with the likely candidates for a polysilicon 'ink'. Furthermore, the mechanical properties of poly-Si are not compatible with advantages that are generally attributed to the use of flexible substrates as poly-Si films tend to be brittle [40–42]. Amorphous Si has been successfully printed using the inkjet printing method, but the device performance of the amorphous Si is extremely poor compared to the poly-Si [40, 41].

The fabrication of a number of materials has been attempted through the inkjet printing process in order to realize a true printed solar cell. The focus of most of these efforts to print solar cells has been on the inorganic materials due to their robust nature and many interesting properties. The inorganic materials that have been successfully printed using an inkjet printer are nanoparticles of Cu, Ag, Au, ZnO, $CuInS_2$ (CIS), $CuInGaS_2$ (CIGS), multiwall carbon nanotubes, and single wall carbon nanotubes [40, 43–45]. Organic materials have also been successfully printed using inkjet printing methods with polyvinylphenol, polyimide, acryl-based polymers, polypyrrole, and poly(3,4 ethylenedioxythiophene) among the extensive list of examples [45, 46]. Yet organic semiconductors tend to be more sensitive to environmental degradation and efficiencies remain extremely low and thus are not ideal as solar materials [46]. All of the materials mentioned above, while successfully printed using an inkjet printer, nonetheless required a post printing treatment [44].

Solution-processed perovskites, on the other hand, can be used as inks for inkjet printing thus making the inorganic quantum dots of the inorganic halide-based perovskites scalable [47], therein lies a major advantage of the quantum dots of the inorganic halide-based perovskites. It is important to mention that this has been reduced to practice [48], although we note, it is not the same perovskite as discussed here. Indeed, as discussed herein, the printed quantum dots of the inorganic halide-based perovskites may in fact exhibit improved performance. Many inorganic solar materials have been printed using inkjet printing, as mentioned above, but to the best of our knowledge no group has yet reported printing thin films of quantum dots of the inorganic halide-based perovskite semiconductors which were actually printed with an inkjet printer with no post printing heat treatment. A successful implementation of low-temperature solution based inorganic perovskite QDs is the next exciting step for inkjet printed solar cells.

## Methods

The $CsPbBr_3$ quantum dots were synthesized under a $N_2$ environment. A schematic of the quantum dot synthesis process can be seen in figure 1(a). Cesium oleate was first
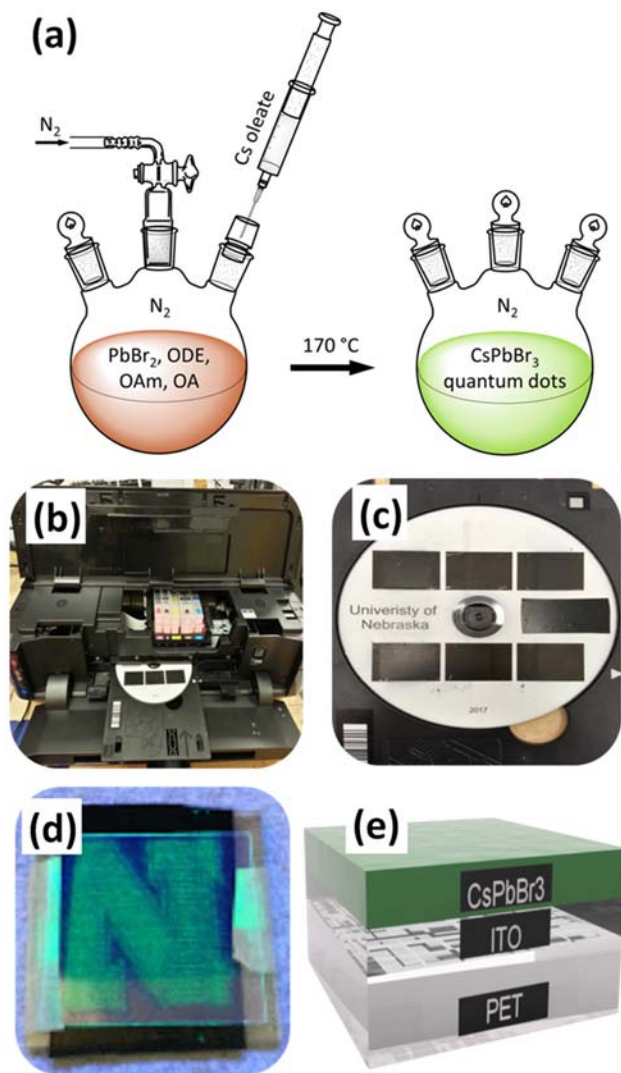
**Figure 1.** (a) Cartoon of CsPbBr$_3$ quantum dot (QD) ink synthesis, synthesis of precursor cesium oleate, cesium oleate is injected into PbBr$_2$, ODE, OAm, OA precursor solution, CsPbBr$_3$ QDs crystallize at around 170° C and are extracted with a syringe, (b) photo of canon inkjet printer with the perovskite inks and printing template loaded, (c) photo of printing template loaded into CD tray of printer, (d) University of Nebraska 'N' printed design with luminescent CsPbBr$_3$ QD ink, (f) cartoon of solar cell structure, CsPbBr$_3$ QD thin film is printed onto indium tin oxide (ITO) coated polyethylene terephthalate (PET) flexible substrate.

synthesized under N$_2$ environment. 0.203 g of cesium carbonate (Cs$_2$CO$_3$), 10 ml of octadecene (ODE), and 1.025 ml of oleic acid (OA) were added to a flask and the mixture was then heated to 150 °C and stirred until the Cs$_2$CO$_3$ fully dissolved. Then the mixture was kept in N$_2$ environment and the temperature was lowered to 100 °C to avoid precipitation and decomposition of the cesium oleate.

37.5 ml of ODE, 7.5 ml of oleylamine(OAm), 3.75 ml of OA and 1.35 mmol of PbBr$_2$ were mixed, stirred, and heated to 100 °C and then allowed to degas for 10 min until the PbBr$_2$ dissolved. A rubber septum was added to the round bottom flask and the mixture was heated to 170 °C. After the mixture reached 170 °C (dark yellow color), 1.375 ml of cesium

oleate was injected quickly via glass syringe through the rubber septum. After 5 s, the three-neck round bottom flask was cooled using an ice/water bath. The quantum dots were then separated using a centrifuge at 5000 rpm for 5 min. 25 ml of acetone was added to the supernatant and re-centrifuged under the same conditions. The separated quantum dots were then dissolved in 25 ml of hexanes. This solution was then used as an ink in the inkjet printer cartridges for printing thin films.

A Canon Pixma iP7220 inkjet printer was used to print all the quantum dot thin films of the inorganic halide-based perovskites, as shown in figure 1(b). Indium tin oxide (ITO) coated polyethylene terephthalate (PET) flexible substrates or amorphous glass substrates were used as printing surfaces. The substrates were cleaned in an acetone wash followed by methanol, methanol was used in order to remove acetone residues. The ITO/PET or amorphous glass substrates were attached to a compact disc and then inserted into the inkjet printer's CD tray, as shown in figure 1(c). The thin films of CsPbBr$_3$ quantum dots were printed onto the substrates and checked for proper luminescence as seen in figures 1(d) and (e). A detailed description of the CsPbBr$_3$ quantum dots inks and further characterization was reported in an earlier publication, for interested readers please see the work published by Shekhirev *et al* [12]. Throughout this work, a film printed in one pass on the substrate is referred to as single layer, although the film thickness is tens of nanometers thick. Likewise, a double layer film consists of two passes from the inkjet printer. Because of the high temperature generated in the printing process, we expect the morphology of this single layer to differ from the 'double' layer, or twice printed, films.

X-ray diffraction (XRD) characterization of the quantum dots thin films of the inorganic halide-based perovskites was performed on a PANanalytical Empyrean diffractometer using a Cu-K$_\alpha$ source with a wavelength of 1.54 Å. All XRD was performed in air at room temperature. The *I–V* measurements were performed through the use of a Keithley 2411B SourceMeter to supply a dc voltage, a Keithley 6485 PicoAmmeter to measure the current, and an HP 3478A Multimeter to measure the voltage across the devices.

The *C–V* measurements were performed using an HP model 4192A impedance analyzer with an oscillation voltage set to 5 mV. All *C–V* measurements were performed at 10 kHz frequency. All *I–V* and *C–V* measurements were performed in air at room temperature. The *I–V* and *C–V* measurements were taken on multiple samples (and found to be highly reproducible) both in the dark, with no illumination, and then under a 26 W Hg lamp with a wavelength of 425 nm and a light intensity of 14.1 mW cm$^{-2}$. To establish that the quantum dots retained the local bond order expected of the inorganic halide-based perovskite, x-ray photoelectron spectroscopy (XPS) was performed with a VG-100 hemispherical analyzer, with a constant analyzer pass energy of 23.5 eV, using non-monochromatized Al-K$_\alpha$ x-ray radiation. The XPS spectra were further analyzed using the XPST curve fitting package in Igor Pro. The XPS spectra binding energies are referenced to the C 1s peak centered at 284.6 eV.

## Results and discussion

The XRD results indicate that the crystalline $CsPbBr_3$ QD inks are robust, and the perovskite structure is established after the inkjet printing process. The XRD data, as seen in figure 2, indicates the as-synthesized (dropcast) $CsPbBr_3$ QD inks are in the orthorhombic room temperature phase for $CsPbBr_3$ perovskite, in good agreement with reports in literature [22, 49, 50]. In conjunction with the Scherrer equation and a standard Lorentzian fitting function of the (220) Bragg peak, the QD size for the dropcast films has been determined to be around 5.5 nm [51]. It is important to note that a shape factor, $k = 0.89$, was used based on an earlier publication indicating that these QDs are cube like nanoparticles.

The inkjet printer in this study uses a current pulse to heat a resistor which then, in turn, heats the ink. Thus in the inkjet printing process, the ink is super-heated well above its boiling point and begins to form bubbles, vaporizing the ink. The bubble expands, forcing ink out of a nozzle and this in turn forms an ink droplet. The details of this process are beyond the scope of this manuscript, but for interested readers a thorough discussion may be found in the literature [41, 45, 46, 52, 53]. The process of super heating the inks to form bubble nucleation involves high temperatures over a short period of time, 10 $\mu$s [53]. The $CsPbBr_3$ QD ink undergoes a dramatic change in texture following this printing process. The printed layers adopt a (110) texture growth, as is evident from the (110) and (220) crystal planes of $CsPbBr_3$ perovskite. The high intensity and broad x-ray scattering feature located around 24 degrees, in both the single and double layer printed thin films, are due to the underlying amorphous glass substrates used for the XRD samples. A peak located around 13 degrees in the double layer thin film is due to segregated $PbBr_2$ precursor. Because of the high temperatures and short time scale associated with droplet formation in the printing process, as noted above, differences between the single layer and double layer printed films are expected. These latter differences in morphology and composition should, in turn, affect the drift carrier lifetime, as is indeed seen, as discussed below.

Using the Scherrer equation and a Lorentzian fitting function for the (220) x-ray diffraction peaks, as plotted in figure 2, the quantum dot sizes were determined to be similar for the single and double layer films. As the printed films were not post-annealed it is safe to assume that the textural change observed is solely due to the inkjet printing process. Further study is required to understand the exact mechanisms mediating the changes in crystallinity before and after the inkjet printing process.

The XPS spectra for single layer printed $CsPbBr_3$ is shown in figure 3. The Cs $3d_{5/2}$ and $3d_{3/2}$ core level peaks are shown in figure 3(a) and are located at binding energies ($E_F$-$E$) of $723.8 \pm 0.2$ eV and $737.85 \pm 0.2$ eV, respectively. The Pb $4f_{7/2}$ and $4f_{5/2}$ core level photoemission features, shown in figure 3(b), located at binding energies of $138.1 \pm 0.1$ eV and $142.9 \pm 0.2$ eV, respectively. The Br $3d_{5/2}$ and $3d_{3/2}$ are not resolved, contributing to a single core level photoemission feature, centered around a binding energy of 68 eV, as shown in figure 3(c). Upon further analysis of the Br 3d core level
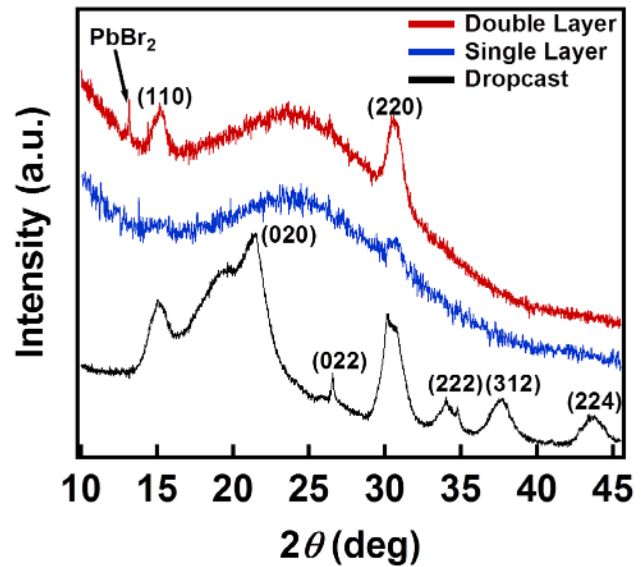


**Figure 2.** X-ray diffraction measurements of the as synthesized $CsPbBr_3$ QD ink (black curve), inkjet printed $CsPbBr_3$ QD single layer film (blue curve), inkjet printed $CsPbBr_3$ QD double layer film (red curve).

photoemission feature, by peak fitting with a Voigt function, we determined that the Br $3d_{5/2}$ binding energy is centered at 68.1 eV, while the $3d_{3/2}$ peak is centered at 69.6 eV. Interestingly, there are two additional peaks, centered at $75.1 \pm 0.2$ eV and $77.1 \pm 0.2$ eV, in the Br 3d spectrum which are due to Cs $4d_{5/2}$ and $4d_{3/2}$ core levels, respectively. All peaks for Cs, Pb, and Br agree well with reported literature values for a $CsPbBr_3$ perovskite structure further confirming, in conjunction with XRD, the films are of high quality and experience no degradation after exposure to ambient conditions [16, 50, 54, 55].

We do not observe extra peaks, in the Pb $4f_{7/2}$ and $4f_{5/2}$ core level photoemission, that might be attributable to metallic Pb clusters. The bonding environments of the Cs, Pb, and Br constituents were investigated with XPS. It is known that the hybrid organic lead halide-based perovskites are prone to the surface segregation of metallic Pb clusters after radiation exposure [56–61]. The segregated metallic Pb clusters show up in XPS spectra as extra peaks and can act as a sign of degradation and poor film quality, but this does not occur here.

A fundamental process of semiconductor device physics is carrier generation and recombination. With the goal of understanding the charge carrier transport dynamics, under working conditions, $I$–$V$ and $C$–$V$ measurements were taken for each printed layer in dark and light conditions, as shown in figure 4. Both the single layer and double layer $CsPbBr_3$ films showed very low dark currents across the entire applied voltage range as evidenced from the blue curves in the $I$–$V$ plots of figures 4(a) and (c). The dark current in the single and double layer films were measured to be 1.11 pA and 1.07 pA at 1.0 V applied voltage, respectively. Very low dark currents are essential for application as photodetectors, as this allows for the device to achieve high signal-to-noise ratios [62]. Furthermore, the low dark current is indicative of a low charge carrier concentration and a well-compensated semiconductor, in the absence of photo-induced carriers [63].
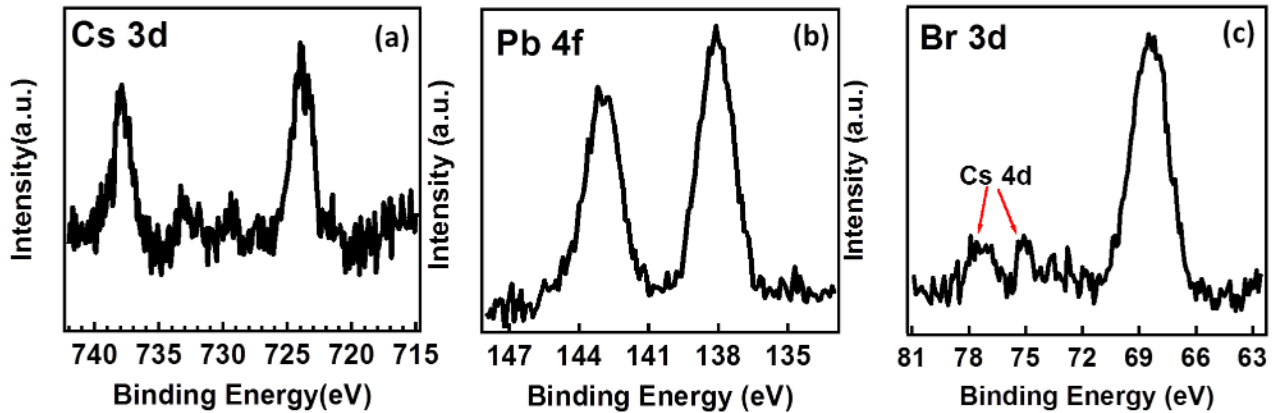
**Figure 3.** X-ray photoelectron spectroscopy of (a) the Cs 3d peaks, (b) Pb 4f peaks, and (c) the Br 3d peak and Cs 4d peaks for the CsPbBr$_3$ QD single layer thin films.
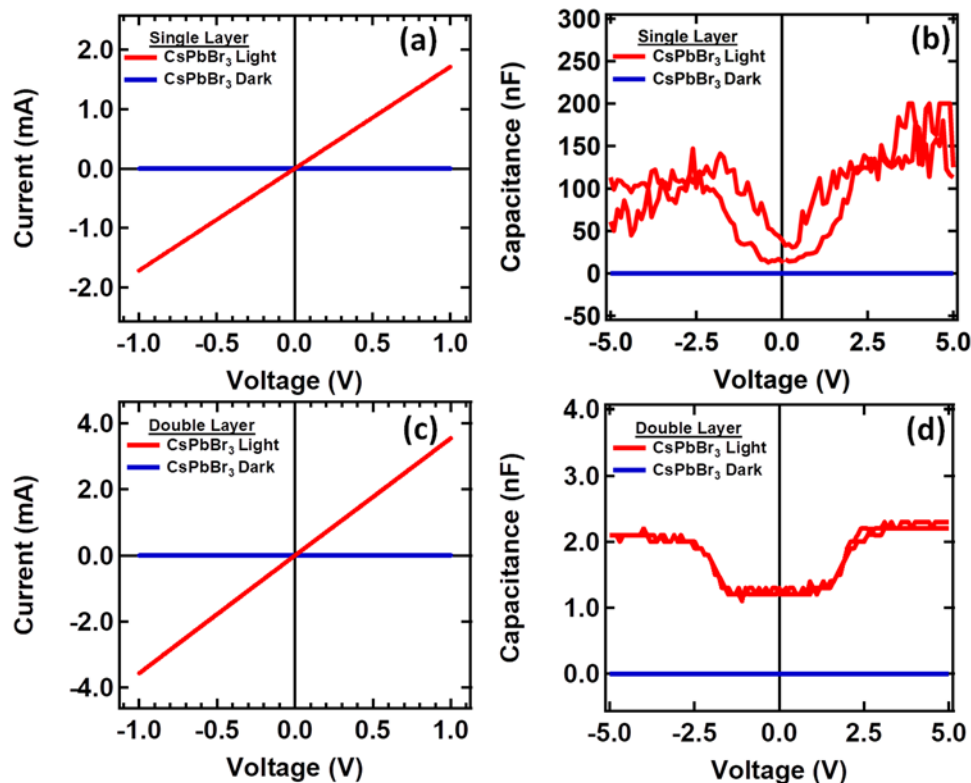


**Figure 4.** Transport measurements in dark (blue curves) and under light illumination (red curves), (a) $I$–$V$ measurements for single layer CsPbBr$_3$, (b) $C$–$V$ measurements for single layer CsPbBr$_3$, (c) $I$–$V$ measurements for double layer CsPbBr$_3$, (d) $C$–$V$ measurements for double layer CsPbBr$_3$.

Under light illumination fluences of 14.1 mW cm$^{-2}$, the measured current rises linearly to 1.71 mA at 1.0 V applied voltage which implies a photocarrier to dark current on/off ratio of $1.54 \times 10^9$ for the single layer printed CsPbBr$_3$ films. For the double layer printed CsPbBr$_3$ films, a measured current of 3.55 mA at 1.0 V applied voltage under light illumination was observed and provides an on/off ratio of $3.55 \times 10^9$. These astonishingly high on/off ratios, greater than $1 \times 10^9$, are several orders of magnitude larger than the highest reported literature values to date, for solution processed CsPbBr$_3$ QDs [55, 63]. The appearance of a significant non-zero current, under light illumination, indicates that both films are photoactive. Furthermore, the roughly linear

$I$–$V$ characteristics under light illumination in both the single printed layer film and double printed layer film devices indicate that a good ohmic contact has been made. The linearity of the data, rather the lack of kinks and absence of hysteresis in the $I$–$V$ curves under illumination, also suggests that there is negligible ion migration present [3, 63]. If significant ion migration were present it is expected that the internal field would change and thus show up as kinks or hysteresis in the $I$–$V$ curves. The presence of hysteresis in the $I$–$V$ curves of the halide-based perovskites impedes the realization of a viable large scale commercialization [3]. Hysteresis is not typical of the inorganic perovskites, so the absence of hysteresis is desirable.
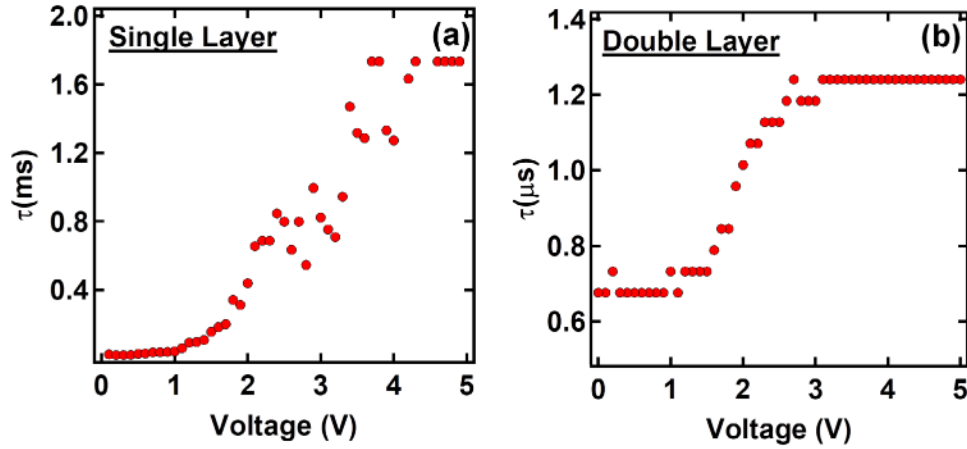
**Figure 5.** Carrier lifetime extracted from the *I–V* and *C–V* data of figure 4, with illumination. Bias voltage lifetimes on the order of (a) a couple of milliseconds for single layer and (b) on the order of a couple of microseconds for the double layer films are estimated.

As can be seen in figures 4(b) and (d), both films experience extremely low capacitance under dark conditions, once again, indicating a very low density of carriers, in agreement with the dark *I–V* measurements. Under light illumination the zero-bias measured capacitance increases to 14 nF in the single layer films while in the double layer film the zero-bias measured capacitance increases to 1.2 nF. The existence of capacitance at zero-bias under light illumination is another indication of charge separation due to formation of excitons, which have been separated to the electrodes. The large difference, by more than an order of magnitude, of the capacitance between the single layer printed films versus the double layer printed films, as is evident in figures 4(b) and (d), suggests morphology is key to the long drift carrier lifetimes, as discussed below. The single layer printed films have capacitance on the order of hundreds of nanoFarads, at higher bias, indicating extremely efficient charge carrier separation, but this capacitance falls at low bias. By way of comparison, the double layer films show only a few nanoFarads of capacitance at high bias indicating the charge separation efficiency, or the photocarrier lifetimes are lower compared to the single layer printed films. Both films indicate a decreased capacitance and current death at low bias which is indicative of substantially reduced carrier concentrations, possibly a result of recombination, or inefficient exciton unbinding in this region of low bias, as is also evident from the photocarrier drift lifetime, discussed below.

The *I–V* and *C–V* data were used to extract an effective carrier lifetime for the single and double layer films following methods discussed in studies performed by Echeverria *et al* [64] and Peterson *et al* [65]. The low frequency conductance, $G_0$, can be defined as [66]:

$$G_0 = \frac{\mathrm{d}I}{\mathrm{d}V_a} \tag{1}$$

where $I$ is the measured current and $V_a$ is the applied voltage. The slope of the *I–V* curves in figures 4(a) and (c) can thus be viewed as the low frequency conductance. It is vital to mention that $G_0$ is dependent on the carrier concentration, built in voltage, doping profile, and carrier lifetime. The frequency

dependent diffusion capacitance, $C_D$, is defined as follows [67]:

$$C_D = \frac{G_0}{\omega\sqrt{2}}\left(\sqrt{1+\omega^2\tau^2}-1\right)^{\frac{1}{2}} \tag{2}$$

where $\omega = 2\pi f$ is the angular frequency, $f$ is the driving frequency, and $\tau$ is the drift carrier lifetime, rather the effective carrier lifetime. Solving equation (2) for $\tau$ gives the effective carrier life time as:

$$\tau = \frac{\left(\left(\left(\frac{C_D\omega\sqrt{2}}{G_0}\right)^2+1\right)^2-1\right)^{\frac{1}{2}}}{\omega}. \tag{3}$$

Using equation (3), the extracted effective carrier lifetime versus voltage has been plotted out for the single layer and double layer films as shown in figures 5(a) and (b), respectively. The dark carrier lifetimes for the single layer and double layer films were estimated to be in the region of 49.7 ns and 15.7 ns, respectively, based on the *I–V* and *C–V* data of figure 4. Under illumination, we find that the photocarrier lifetime is far higher, but begins to die off for both the single and double layer films, at low bias voltages, <2 V. Deep trap states could act as recombination centers for non-radiative recombination of the charge carriers. It is at low bias voltage that the influence of deep trap states is most profound, as hot carrier transport is less dominant. It has been suggested that deep trap states result in Shockley–Read–Hall (SRH) non-radiative recombination, also known as trap-assisted recombination, which leads to poor photovoltages and hence low power conversion efficiency in halide-based perovskites [3, 68–70]. Deep trap states generally shorten the non-radiative lifetime of charge carriers. Kang and Wang [71] showed that the most probable deep trap state formed in $CsPbBr_3$ is due to $PbBr_2$ defects.

At high bias voltages, i.e. >2 V, the lifetimes increase until saturation occurs, around 3–4 V applied bias voltage. In this region the excitons unbind leading to well separated electron-hole pairs and better carrier sweep out. The saturation of the photocarrier drift lifetime may be due to trapping by shallow

trap states or surface states located near the band edges, but no definitive explanation is available from this data. In these shallow trap states or surface states, carriers become trapped for some time and then must be injected back into the band edge before recombination can occur hence the longer lifetimes [70]. In the study by Kang and Wang [71] many defects produced in $CsPbBr_3$ induced shallow states with Cs vacancies having the lowest formation energy and thus being the most stable and probable contributor to shallow states. The more interesting observation is the stark difference in the magnitude of the lifetimes when the single layer films are compared to the double layer films. The single layer printed thin films have photocarrier lifetimes on the order of a couple milliseconds whereas the double layer thin films have photocarrier lifetimes on the order of just a couple microseconds. The long carrier lifetimes of the single layer films are about 40 times longer than the highest lifetimes of inorganic perovskite films reported in literature, which have ranged from 3.9 ns–50 $\mu$s [9–11, 72]. To our knowledge the highest reported effective carrier lifetime is for single crystal organic–inorganic-halide-based perovskites and it is on the order of a few milliseconds [73].

A possible explanation for the large difference between single layer printed film and double layer printed film lifetimes might be the result of changing quantum dot morphology, or possibly changing interface morphology, not present in the single layer films. There is also the possibility that $PbBr_2$ could be acting as a defect state, deep trap state, which is more favorable for fast recombination and thus shorter effective carrier lifetimes. Furthermore, as we are comparing a single printed layer versus a twice printed layer it could be inferred that a critical thickness exists whereby the transport properties are more favorable when the printed film thickness is below said critical thickness. More detailed studies are needed to understand the role of the film morphology, the $PbBr_2$ defects, and film thickness as they apply to the carrier transport and overall device optimization.

## Conclusion

This study demonstrates the potential of inkjet printing for mass production of high quality photoactive inorganic perovskite QD films. The printed films result in a different crystallographic texture than the as prepared inks, but XRD and XPS confirm the perovskite structure and quality is robust and survives the printing process. Through transport measurements it is evident that the resulting films have effective photocarrier drift lifetimes on the order of a couple of milliseconds and on/off ratios greater than $10^9$. These extraordinary results show the great promise of the inorganic halide-based perovskites for use in photovoltaic devices and as inks in inkjet printing methods. The key point is that these are very long drift carrier lifetimes for a defective semiconductor. As such this is somewhat unexpected, but more importantly, it will no doubt influence charge collection efficiencies in the perovskites. The fact that the 'printed' quantum dots are uniform as well as have a high textured orientation with respect to the film normal, means that in applications involving displays, the luminescence is far more likely to be uniform and thus more valuable when reduced to practice.

## Author contributions

CCI, PAD, and AJY designed the experiment and wrote the manuscript. AJY analyzed the data sets. CCI and AJY calculated the lifetimes. AJY made the figures. FG and PSC printed the thin films. BLS and NB performed the *I–V* and *C–V* measurements. IRE performed the XPS. JDT and MS synthesized the inks. JDT performed the XRD. SS, AE, PAD and AS developed the original printing method with other inks. All authors contributed to the writing of this manuscript.

## ORCID iDs

P A Dowben https://orcid.org/0000-0002-2198-4710
A J Yost https://orcid.org/0000-0002-6220-7520

## References

[1] Kojima A, Teshima K, Shirai Y and Miyasaka T 2009 Organometal halide perovskites as visible-light sensitizers for photovoltaic *J. Am Chem. Soc.* **131** 6050–1

[2] National Renewable Energy Laboratory (NREL) 2018 Solar Cell Efficiency Records as of 15 March 2018 (www.energy.gov/eere/solar/downloads/research-cell-efficiency-records)

[3] Li C, Guerrero A, Zhong Y and Huettner S 2017 Origins and mechanisms of hysteresis in organometal halide perovskites *J. Phys.: Condens. Matter* **29** 193001

[4] Chen Z, Wang J J, Ren Y, Yu C and Shum K 2012 Schottky solar cells based on CsSnI $_3$ thin-films *Appl. Phys. Lett.* **101** 93901

[5] Kumar M H *et al* 2014 Lead-free halide perovskite solar cells with high photocurrents realized through vacancy modulation *Adv. Mater.* **26** 7122–7

[6] Swarnkar A, Marshall A R, Sanehira E M, Chernomordik B D, Moore D T, Christians J A, Chakrabarti T and Luther J M 2016 Quantum dot–induced phase stabilization of a-CsPbI3 perovskite for high-efficiency photovoltaics *Science* **354** 92–6

[7] Chen C Y, Lin H Y, Chiang K M, Tsai W L, Huang Y C, Tsao C S and Lin H W 2017 All-vacuum-deposited stoichiometrically balanced inorganic cesium lead halide perovskite solar cells with stabilized efficiency exceeding 11% *Adv. Mater.* **29** 1–7

[8] Sanehira E M, Marshall A R, Christians J A, Harvey S P, Ciesielski P N, Wheeler L M, Schulz P, Lin L Y, Beard M C and Luther J M 2017 Enhanced mobility CsPbI3 quantum dot arrays for record-efficiency, high-voltage photovoltaic cells *Sci. Adv.* **3** eaao4204

[9] Yantara N, Bhaumik S, Yan F, Sabba D, Dewi H A, Mathews N, Boix P P, Demir H V and Mhaisalkar S 2015

Inorganic halide perovskites for efficient light-emitting diodes *J. Phys. Chem. Lett.* **6** 4360–4

[10] Rakita Y, Kedem N, Gupta S, Sadhanala A, Kalchenko V, Böhm M L, Kulbak M, Friend R H, Cahen D and Hodes G 2016 Low-temperature solution-grown CsPbBr$_3$ single crystals and their characterization *Cryst. Growth Des.* **16** 5717–25

[11] Hutter E M, Sutton R J, Chandrashekar S, Abdi-Jalebi M, Stranks S D, Snaith H J and Savenije T J 2017 Vapour-deposited cesium lead iodide perovskites: microsecond charge carrier lifetimes and enhanced photovoltaic performance *ACS Energy Lett.* **2** 1901–8

[12] Shekhirev M, Goza J, Teeter J, Lipatov A and Sinitiskii A 2017 Synthesis of cesium lead halide quantum dots *J. Chem. Educ.* **94** 1150–6

[13] Protesescu L, Yakunin S, Bodnarchuk M I, Krieg F, Caputo R, Hendon C H, Yang R X, Walsh A and Kovalenko M V 2015 Nanocrystals of cesium lead halide perovskites (CsPbX$_3$, X = Cl, Br, and I): novel optoelectronic materials showing bright emission with wide color gamut *Nano Lett.* **15** 3692–6

[14] Song J, Li J, Li X, Xu L, Dong Y and Zeng H 2015 Quantum dot light-emitting diodes based on inorganic perovskite cesium lead halides (CsPbX$_3$) *Adv. Mater.* **27** 7162–7

[15] Wang Y, Li X, Song J, Xiao L, Zeng H and Sun H 2015 All-inorganic colloidal perovskite quantum dots: a new class of lasing materials with favorable characteristics *Adv. Mater.* **27** 7101–8

[16] Endres J, Kulbak M, Zhao L, Rand B P, Cahen D, Hodes G and Kahn A 2017 Electronic structure of the CsPbBr$_3$/polytriarylamine (PTAA) system *J. Appl. Phys.* **121** 35304

[17] Jeong B, Han H, Choi Y J, Cho S H, Kim E H, Lee S W, Kim J S, Park C, Kim D and Park C 2018 All-inorganic CsPbI$_3$ perovskite phase-stabilized by poly(ethylene oxide) for red-light-emitting diodes *Adv. Funct. Mater.* 1706401

[18] Pan J *et al* 2018 Bidentate ligand-passivated CsPbI$_3$ perovskite nanocrystals for stable near-unity photoluminescence quantum yield and efficient red light-emitting diodes *J. Am. Chem. Soc.* **140** 562–5

[19] Dursun I *et al* 2016 Perovskite nanocrystals as a color converter for visible light communication *ACS Photonics* **3** 1150–6

[20] Mei S, Liu X, Zhang W, Liu R, Zheng L, Guo R and Tian P 2018 High-bandwidth white-light system combining a micro-LED with perovskite quantum dots for visible light communication *ACS Appl. Mater. Interfaces* **10** 5641–8

[21] Li G *et al* 2016 Highly efficient perovskite nanocrystal light-emitting diodes enabled by a universal crosslinking method *Adv. Mater.* **28** 3528–34

[22] Eaton S W, Lai M, Gibson N A, Wong A B, Dou L, Ma J, Wang L-W, Leone S R and Yang P 2016 Lasing in robust cesium lead halide perovskite nanowires *Proc. Natl Acad. Sci.* **113** 1993

[23] Yakunin S *et al* 2015 Low-threshold amplified spontaneous emission and lasing from colloidal nanocrystals of caesium lead halide perovskites *Nat. Commun.* **6** 1–8

[24] Fu Y, Zhu H, Stoumpos C C, Ding Q, Wang J, Kanatzidis M G, Zhu X and Jin S 2016 Broad wavelength tunable robust lasing from single-crystal nanowires of cesium lead halide perovskites (CsPbX$_3$, X = Cl, Br, I) *ACS Nano* **10** 7963–72

[25] Zhou H *et al* 2017 Vapor growth and tunable lasing of band gap engineered cesium lead halide perovskite micro/nanorods with triangular cross section *ACS Nano* **11** 1189–95

[26] Tang B, Dong H, Sun L, Zheng W, Wang Q, Sun F, Jiang X, Pan A and Zhang L 2017 Single-mode lasers based on

cesium lead halide perovskite submicron spheres *ACS Nano* **11** 10681–8

[27] Huang C-Y, Zou C, Mao C, Corp K L, Yao Y-C, Lee Y-J, Schlenker C W, Jen A K-Y and Lin L 2017 CsPbBr$_3$ perovskite quantum dot vertical cavity lasers with low threshold and high stability *ACS Photonics* **4** 2281–9

[28] Evans T J S, Schlaus A, Fu Y, Zhong X, Atallah T L, Spencer M S, Brus L E, Jin S and Zhu X Y 2018 Continuous-wave lasing in cesium lead bromide perovskite nanowires *Adv. Opt. Mater.* **6** 1–7

[29] Hu Z *et al* 2017 Robust cesium lead halide perovskite microcubes for frequency upconversion lasing *Adv. Opt. Mater.* **5** 1–8

[30] Shoaib M *et al* 2017 Directional growth of ultralong CsPbBr$_3$ perovskite nanowires for high-performance photodetectors *J. Am. Chem. Soc.* **139** 15592–5

[31] Zheng W, Xiong X, Lin R, Zhang Z, Xu C and Huang F 2017 Balanced photodetection in one-step liquid-phase synthesis CsPbBr$_3$ micro/nanoflake single crystal *ACS Appl. Mater. Interfaces* **10** 1865–70

[32] Ding J, Du S, Zuo Z, Zhao Y, Cui H and Zhan X 2017 High detectivity and rapid response in perovskite CsPbBr$_3$ single-crystal photodetector *J. Phys. Chem.* C **121** 4917–23

[33] Dirin D N, Cherniukh I, Yakunin S, Shynkarenko Y and Kovalenko M V 2016 Solution-grown CsPbBr$_3$ perovskite single crystals for photon detection *Chem. Mater.* **28** 8470–4

[34] Stoumpos C C *et al* 2013 Crystal growth of the perovskite semiconductor CsPbBr$_3$: a new material for high-energy radiation detection *Cryst. Growth Des.* **13** 2722–7

[35] Eperon G E, Paternò G M, Sutton R J, Zampetti A, Haghighirad A A, Cacialli F and Snaith H J 2015 Inorganic caesium lead iodide perovskite solar cells *J. Mater. Chem.* A **3** 19688–95

[36] Shahiduzzaman M, Yonezawa K, Yamamoto K, Ripolles T S, Karakawa M, Kuwabara T, Takahashi K, Hayase S and Taima T 2017 Improved reproducibility and intercalation control of efficient planar inorganic perovskite solar cells by simple alternate vacuum deposition of PbI$_2$ and CsI *ACS Omega* **2** 4464–9

[37] Frolova L A, Anokhin D V, Piryazev A A, Luchkin S Y, Dremova N N, Stevenson K J and Troshin P A 2017 Highly efficient all-inorganic planar heterojunction perovskite solar cells produced by thermal coevaporation of CsI and PbI$_2$ *J. Phys. Chem. Lett.* **8** 67–72

[38] Kulbak M, Cahen D and Hodes G 2015 How important is the organic part of lead halide perovskite photovoltaic cells? Efficient CsPbBr$_3$ cells *J. Phys. Chem. Lett.* **6** 2452–6

[39] Teng K F and Vest R W 1988 Application of ink jet technology on photovoltaic metallization *IEEE Electron Device Lett.* **9** 591–3

[40] Habas S E, Platt H A S, van Hest M F A M and Ginley D S 2010 Low-cost inorganic solar cells: from ink to printed device *Chem. Rev.* **110** 6571–94

[41] Leenen M A M, Arning V, Thiem H, Steiger J and Anselmann R 2009 Printable electronics: flexibility for the future *Phys. Status Solidi* **206** 588–97

[42] Stüwe D, Mager D, Biro D and Korvink J G 2015 Inkjet technology for crystalline silicon photovoltaics *Adv. Mater.* **27** 599–626

[43] Wang W, Su Y W and Chang C H 2011 Inkjet printed chalcopyrite CuIn$_x$Ga$_{1-x}$Se$_2$ thin film solar cells *Sol. Energy Mater. Sol. Cells* **95** 2616–20

[44] Azimi H, Hou Y and Brabec C J 2014 Towards low-cost, environmentally friendly printed chalcopyrite and kesterite solar cells *Energy Environ. Sci.* **7** 1829–49

[45] Yin Z P, Huang Y A, Bu N B, Wang X M and Xiong Y L 2010 Inkjet printing for flexible electronics: materials, processes and equipments *Chin. Sci. Bull.* **55** 3383–407

[46] Tekin E, Smith P J and Schubert U S 2008 Inkjet printing as a deposition and patterning tool for polymers and inorganic particles *Soft Matter* **4** 703–13

[47] Song J, Xu L, Li J, Xue J, Dong Y, Li X and Zeng H 2016 Monolayer and few-layer all-inorganic perovskites as a new family of two-dimensional semiconductors for printable optoelectronic devices *Adv. Mater.* **28** 4861–9

[48] Suale Technologies Inkjet printing (http://sauletech.com/technology/)

[49] Koolyk M, Amgar D, Aharon S and Etgar L 2016 Kinetics of cesium lead halide perovskite nanoparticle growth; focusing and de-focusing of size distribution *Nanoscale* **8** 6403–9

[50] Palazon F, Di Stasio F, Lauciello S, Krahne R, Prato M and Manna L 2016 Evolution of CsPbBr$_3$ nanocrystals upon post-synthesis annealing under an inert atmosphere *J. Mater. Chem.* C **4** 9179–82

[51] Scherrer P 1918 Bestimmung der Größe und der inneren Struktur von Kolloidteilchen mittels Röntgenstrahlen *Nachr. Ges. Wiss. Göttingen* **2** 98–100

[52] Pace G, Grimoldi A, Sampietro M, Natali D and Caironi M 2015 Printed photodetectors *Semicond. Sci. Technol.* **30** 104006

[53] Hawkins W G 1985 Bubble jet printing device *US Patent* No. 4,523,530 (Xerox Corp)

[54] Begum R, Parida M R, Abdelhady A L, Murali B, Alyami N M, Ahmed G H, Hedhili M N, Bakr O M and Mohammed O F 2017 Engineering interfacial charge transfer in CsPbBr$_3$ perovskite nanocrystals by heterovalent doping *J. Am. Chem. Soc.* **139** 731–7

[55] Li Y, Shi Z-F, Li S, Lei L-Z, Ji H-F, Wu D, Xu T-T, Tian Y-T and Li X-J 2017 High-performance perovskite photodetectors based on solution-processed all-inorganic CsPbBr$_3$ thin films *J. Mater. Chem.* C **5** 8355–60

[56] Conings B, Baeten L, De Dobbelaere C, D'Haen J, Manca J and Boyen H-G 2014 Perovskite-based hybrid solar cells exceeding 10% efficiency with high reproducibility using a thin film sandwich approach *Adv. Mater.* **26** 2041–6

[57] Lindblad R *et al* 2015 Electronic structure of CH$_3$NH$_3$PbX$_3$ perovskites: dependence on the halide moiety *J. Phys. Chem.* C **119** 1818–25

[58] Zu F, Amsalem P, Salzmann I, Wang R, Ralaiarisoa M, Kowarik S, Duhm S and Koch N 2017 Impact of white light illumination on the electronic and chemical structures of mixed halide and single crystal perovskites *Adv. Opt. Mater.* **5** 1700139

[59] Sadoughi G, Starr D E, Handick E, Stranks S D, Gorgoi M, Wilks R G, Bär M and Snaith H J 2015 Observation and mediation of the presence of metallic lead in organic–inorganic perovskite films *ACS Appl. Mater. Interfaces* **7** 13440–4

[60] Liu P *et al* 2015 Interfacial electronic structure at the CH$_3$NH$_3$PbI$_3$/MoO$_x$ interface *Appl. Phys. Lett.* **106** 193903

[61] Komesu T *et al* 2016 Surface electronic structure of hybrid organo lead bromide perovskite single crystals *J. Phys. Chem.* C **120** 21710–5

[62] Huang H, Xie Y, Yang W, Zhang F, Cai J and Wu Z 2011 Low-dark-current TiO$_2$ MSM UV photodetectors with Pt schottky contacts *IEEE Electron Device Lett.* **32** 530–2

[63] Saidaminov M I *et al* 2017 Inorganic lead halide perovskite single crystals: phase-selective low-temperature growth, carrier transport properties, and self-powered photodetection *Adv. Opt. Mater.* **5** 1600704

[64] Echeverria E *et al* 2016 Semiconducting boron carbides with better charge extraction through the addition of pyridine moieties *J. Phys. D: Appl. Phys.* **49** 355302

[65] Peterson G G, Echeverria E, Dong B, Silva J P, Wilson E R, Kelber J A, Nastasi M and Dowben P A 2017 Increased drift carrier lifetime in semiconducting boron carbides deposited by plasma enhanced chemical vapor deposition from carboranes and benzene *J. Vac. Sci. Technol.* A **35** 03E101

[66] Pierret R F 1996 *Semiconductor Device Fundamentals* (Reading, MA: Addison-Wesley)

[67] Li S S 2006 *Semiconductor Physical Electronics* (Berlin: Springer)

[68] de Quilettes D W, Vorpahl S M, Stranks S D, Nagaoka H, Eperon G E, Ziffer M E, Snaith H J and Ginger D S 2015 Impact of microstructure on local carrier lifetime in perovskite solar cells *Science* **348** 683–6

[69] Leijtens T, Eperon G E, Barker A J, Grancini G, Zhang W, Ball J M, Kandada A R S, Snaith H J and Petrozza A 2016 Carrier trapping and recombination: the role of defect physics in enhancing the open circuit voltage of metal halide perovskite solar cells *Energy Environ. Sci.* **9** 3472–81

[70] Kiermasch D, Rieder P, Tvingstedt K, Baumann A and Dyakonov V 2016 Improved charge carrier lifetime in planar perovskite solar cells by bromine doping *Sci. Rep.* **6** 1234–7

[71] Kang J and Wang L W 2017 High defect tolerance in lead halide perovskite CsPbBr$_3$ *J. Phys. Chem. Lett.* **8** 489–93

[72] Dastidar S, Li S, Smolin S Y, Baxter J B and Fafarman A T 2017 Slow electron-hole recombination in lead iodide perovskites does not require a molecular dipole *ACS Energy Lett.* **2** 2239–44

[73] Chen Y, Yi H T, Wu X, Haroldson R, Gartstein Y N, Rodionov Y I, Tikhonov K S, Zakhidov A, Zhu X-Y and Podzorov V 2016 Extended carrier lifetimes and diffusion in hybrid perovskites revealed by Hall effect and photoconductivity measurements *Nat. Commun.* **7** 12253